THE JOURNAL OF PHYSICAL CHEMISTRY B

pubs.acs.org/JPCB Article

Energy Transfer across Nonpolar and Polar Contacts in Proteins: Role of Contact Fluctuations

Published as part of The Journal of Physical Chemistry virtual special issue "Yoshitaka Tanimura Festschrift".

Humanath Poudel, Korey M. Reid, Takahisa Yamato, and David M. Leitner*

Cite This: *J. Phys. Chem. B* 2020, 124, 9852−9861 Read Online

ACCESS | Metrics & More | Article Recommendations | Supporting Information

ABSTRACT: Molecular dynamics simulations of the villin headpiece subdomain HP36 have been carried out to examine relations between rates of vibrational energy transfer across noncovalently bonded contacts and equilibrium structural fluctuations, with focus on van der Waals contacts. Rates of energy transfer across van der Waals contacts vary inversely with the variance of the contact length, with the same constant of proportionality for all nonpolar contacts of HP36. A similar relation is observed for hydrogen bonds, but the proportionality depends on contact pairs, with hydrogen bonds stabilizing the α-helices all exhibiting the same constant of proportionality, one that is distinct from those computed for other polar contacts. Rates of energy transfer across van der Waals contacts are found to be up to 2 orders of magnitude smaller than rates of energy transfer across polar contacts.

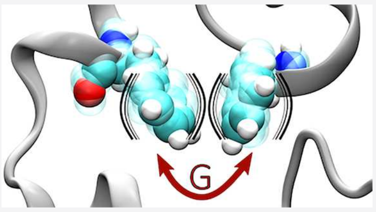

1. INTRODUCTION

Ultrafast time-resolved measurements and computational studies are providing an ever more detailed picture of energy transport in proteins and protein complexes, clarifying connections to the structure and dynamics of proteins and their surroundings.[1−18] These include investigations of energy transfer across individual contacts within or at the interface between biomolecules.[11] Some of those studies have examined relations between equilibrium fluctuations of contacts between protein residues[19−22] as well as residues and water[11,23] and rates of energy transfer across them, suggesting that measurements of energy transfer across inter-residue contacts can provide information about contact dynamics and associated entropy.[11,21,23] In this article, we extend the analysis for the first time to van der Waals contacts for a protein near room temperature. Though rates of energy transfer across nonpolar contacts are often relatively small, a variety of time-resolved spectroscopic experiments probe energy transfer across them,[4,5,15,24−27] motivating analysis of connections to contact dynamics. Here, we examine energy transfer across van der Waals contacts of the 36-residue villin headpiece subdomain (HP36) at 300 K. In addition to analysis of nonpolar contacts, we also compare how rates of energy transfer across polar contacts of HP36 vary with fluctuations in the length of the contact, including hydrogen bonds that stabilize α-helices, neglected in earlier studies of energy transfer and contact dynamics. Energy transfer across hydrogen bonds of the α-helices exhibit a variation with contact fluctuations distinct from other hydrogen bonds within the protein.

The study of vibrational energy relaxation in proteins,[1,2,13,28−32] part of a long-standing goal of describing relaxation dynamics in complex molecular environments,[33−37] has led to a search for relatively simple models that capture its main features. This has included studies addressing the role of structure and bonding, dynamics,[9,31,38−45] and quantum mechanical effects.[46−48] Coarse-grain modeling using a classical master equation offers a promising approach to model energy transport in proteins and protein complexes,[19,20,22] identifying regions along which transport is facile and reproducing energy dynamics quite well when compared with results of all-atom simulations. The master equation simulations support a diffusion-like picture for transport. A diffusion equation describes transport along the backbone; rates of energy transfer in other regions can be estimated by calculation of the local energy diffusivity between residue pairs.[19,20] The combination of transport along the backbone and via nonbonded contacts yields a network for energy transport through the protein,[9,39,40,49−54] influenced by protein structure and geometry as well as its dynamics, and does not necessarily conform to predictions of a contact network.[19,55]

Connections between protein structure and rates of energy transfer along the protein backbone and across some of the polar contacts provide useful information in modeling energy transport in proteins at a coarse-grained level,[21,22] such as master equation simulations, as rate constants that largely mediate energy transport through the protein can often be

Received: September 4, 2020
Revised: October 8, 2020
Published: October 27, 2020

https://dx.doi.org/10.1021/acs.jpcb.0c08091
J. Phys. Chem. B 2020, 124, 9852−9861

estimated from the structure.[22] Nevertheless, there is merit to exploring the relation between the rate constants for energy transfer across contacts and contact dynamics. For one thing, any relation may offer an alternative route to estimating rate constants for master equation simulations, as has been suggested by the results of nonequilibrium and equilibrium MD simulations of HP36 at low temperature.[20] Moreover, for a given contact pair, changes in the rate of energy transfer across a nonbonded contact can be associated with changes in dynamics, and corresponding changes in entropy.[11,21,23]

Contact dynamics may be altered by mutation or change in functional state, yielding a new rate constant for energy transfer across the contact, detectable by time-resolved spectroscopic measurements.[24] For example, in a recent study exploring the relation between dynamics and energy transfer across contacts of the homodimeric hemoglobin (HbI) from *Scapharca inaequivalvis*,[23] ligand binding was found to yield not only more flexible dynamics of contacts between residues and interface water molecules, consistent with the expulsion of water molecules that occurs during the process of ligand binding,[56−59] but also greater flexibility of many other contacts throughout the protein, consistent with findings of earlier computational studies that indicated greater flexibility of the HbI globules upon ligand binding.[60] The dynamics of the protein and partially confined water molecules are coupled and together contribute to allostery of HbI,[61] as has been found for other allosteric proteins.[62] In addition to enhancement of the flexibility and entropy of the globules upon ligand binding, diminished rates of energy transfer across polar contacts of HbI were calculated for the liganded system compared to the unliganded system.[23,61] Measurements of rates of energy transfer across these contacts when ligands are bound and unbound can therefore provide information about changes in the dynamics of the contact and the entropy associated with the dynamics when this change of state occurs.

Until now, we have studied the relation between energy transfer across polar and charged contacts and fluctuations in the length of those contacts at 300 K in myoglobin[21] and HbI.[11,23,61] In those studies, we examined many of the hydrogen bonded contacts between residues, as well as residue−interface water contacts of HbI. In these cases, we have found the rate of energy transfer across the hydrogen bond varies inversely with the variance in the length of the contact. These results are consistent with an earlier study of HP36,[20] where the rate of energy transfer across both hydrogen bonds and van der Waals contacts was found to scale with the inverse of the variance in the length of the contact at low temperatures (about 10 K). Until now, studies of energy transfer across polar contacts and the relation to fluctuations in the length of the contacts have neglected hydrogen bonds that stabilize α-helices, since energy transport along α-helices was found to be dominated by the diffusion equation that governs energy transport along the main chain.[17,63] In this study, we address the relation between rates of energy transfer and dynamics of hydrogen bonds along α-helices.

Besides the short-range van der Waals interactions and hydrogen bonds, we also consider the long-range charged contacts of HP36. In a previous study of charged interactions in myoglobin, the rate of energy transfer across such contacts, when they happen to be very near one another, did not appear proportional to the inverse of the variance in the contact length, likely due to simultaneous and comparable interactions of several charged groups.[21] Energy transfer between charged groups of myoglobin is generally well described by a diffusion equation, consistent with results we find in this study of HP36.

In the following section, we provide information about the computational methods used in this study and theoretical background for analyzing the results. In section 3, we present and discuss the results of the computational studies of energy transfer across nonpolar and polar contacts and their corresponding dynamics, and we conclude in section 4.

2. COMPUTATIONAL METHODS

The initial structure of the villin headpiece, HP36, corresponds to Protein Data Bank (PDB) 1VII. The structure was solvated in an octahedral box with the TIP3P water model, with a solvent radius of 10 Å, using the AMBER ff14SB force field.[64] All of the simulations were carried out using the AMBER16 MD software package.[65] The entire system contains 9871 atoms, of which 596 atoms belong to HP36, 10 Cl^- and 10 Na^+ ions, with the remainder being water molecules. The MD simulations were set up as follows: We performed energy minimization in three successive steps. First, the system was energy minimized over 5000 steps by constraining heavy atoms with a force constant of 90 (kcal mol^{-1})/$Å^2$, relaxing all hydrogen contacts to avoid steric clashes. The second minimization was performed for 5000 steps, in which backbone atoms were constrained with the same force constant as the first. Finally, the system was energy minimized for 5000 steps with position constraints of 2.0 (kcal mol^{-1})/$Å^2$ on all backbone atoms. All minimizations were conducted employing the steepest descent method with a nonbonded cutoff of 9 Å for the particle−particle long-range nonbonded interactions. Periodic boundary conditions were applied for all of the simulations.

To generate the initial velocities of the atoms corresponding to the Maxwell−Boltzmann distribution, a starting temperature of 0.1 K was selected and heated to 300 K over 1 ns. An additional 1 ns simulation was performed holding a constant temperature at 300 K. Heating was conducted under a canonical ensemble using the Berendsen thermostat[66] and applying position constraints on the heavy atoms with a force constant of 2 (kcal mol^{-1})/$Å^2$. The system was integrated every 2.0 fs, and the SHAKE algorithm was applied to constrain all hydrogen-containing bonds to suppress rapid vibration.[67] A temperature time constant of 1.0 ps was applied, allowing for smooth heating. The particle mesh Ewald method was used for electrostatic interactions.

A 2 ns equilibration simulation was performed with a time step of 2 fs under an isobaric−isothermal ensemble (NPT). Heavy atoms were position-constrained with a force constant of 3 (kcal mol^{-1})/$Å^2$. The coupling constants for the barostat and thermostat were 1 and 2 ps, respectively. We further equilibrated the system for 2 ns excluding position restraints, implementing pressure and temperature coupling constants of 1 and 0.5 ps, respectively. An additional 10 ns simulation equilibrated the system under an NPT ensemble with pressure and temperature coupling constants of 0.1 ps.

A sampling simulation of 100 ns was carried out under an NPT ensemble. Each nanosecond, the coordinates and velocities were saved for later microcanonical (NVE) simulations. In this study, the snapshots acquired from 51 to 100 ns, the region showing the greatest stability as determined by the root-mean-square-deviation (RMSD), which remained within 1 Å during this interval, were utilized as starting coordinates and velocities in the NVE simulations. In total, we performed 50 NVE simulations for the analysis of energy conductivity, defined below, and dynamics. Each NVE simulation was allowed to evolve for 500 ps with a time step of 0.5 fs. The corresponding overall average temperature was 301 K with a standard deviation of 2.5 K. The velocity files were saved every 1 fs, and coordinate files were saved every 5 fs. An Ewald sum tolerance of 10^{-7} was applied to reduce energy drift.

Using the trajectories computed for HP36, the residue−residue currents are calculated using CURrent calculation for Proteins (CURP).[3,39,40,45] Starting with the atom−atom energy flow[39]

$$J^k_{i\leftarrow j} = \frac{1}{2}(v_i\cdot F_{ij} - v_j\cdot F_{ji}) \tag{1}$$

where $J^k_{i\leftarrow j}$ is the inter-residue atom−atom energy flow between atoms i and j for trajectory k, v is the velocity, and F is the force of one atom on the other, the inter-residue energy flow is[39]

$$J^k_{A\leftarrow B}(t) = \sum_{i\in A}^{N_A}\sum_{j\in B}^{N_B} J^k_{i\leftarrow j}(t), \tag{2}$$

where N_A (N_B) is the number of atoms in residue A (B). To determine energy currents, L_{AB}, for each pair of residues, an autocorrelation function window of 50 ps was used to evaluate[39]

$$L^k_{AB} = \frac{1}{RT}\lim_{\tau\to\infty}\int_0^\tau \langle J^k_{A\leftarrow B}(t_0)J^k_{A\leftarrow B}(t+t_0)\rangle\, \mathrm{d}t \tag{3}$$

where R is the gas constant and T is the temperature. The chosen time window was sufficient for convergence. We multiply L_{AB} by RT and report values in (kcal mol^{-1})^2 ps^{-1}, yielding G_{AB}, where $G_{AB} = (RT)L_{AB}$, which we refer to as the energy conductivity. We drop subscripts AB in the following. For a residue with excess energy, G quantifies the net energy transferred (multiplied by RT) across a nonbonded contact per unit time. It is proportional to the rate constant for energy transfer across the contact, computed in other studies of energy transport in proteins.[19,20,55] This connection will be discussed further below.

We estimate from G values of rate constants, w, for energy transfer between residues, which are introduced below. As seen in eq 2, G incorporates the number of degrees of freedom of each residue forming the contact, which is squared in eq 3. The energy per degree of freedom can be estimated as the thermal energy, $k_BT/2$, which is also squared in eq 3. On average, there are 57.6 degrees of freedom per residue, or 115.2 degrees of freedom for two residues. Squaring that value and multiplying by $(k_BT/2)^2$ introduces the factor $3318(k_BT)^2$, which at 300 K is 1180 (kcal mol^{-1})^2. We can thereby estimate the rate constant, w, from $w \approx G/[1180\ (\text{kcal mol}^{-1})^2]$. This conversion incorporates the average number of degrees of freedom of an amino acid. For a particular pair of residues, we can adjust this value to account for the degrees of freedom of the specific residue pair, as we do for specific residue pairs below.

Residue pair contacts were taken to be polar, charged, or nonpolar (van der Waals) based upon pair composition. We define polar contacts as X−H···Y, where X and Y are either N or O, having an average distance, H···O, less than 2.8 Å. The subset of polar contacts, hydrogen bonds, have angle, ∠XHO, greater than 150°. The average distance between the O and H involved in the polar contact, $\langle r\rangle$, and variance in the distance, $\langle\delta r^2\rangle = \langle(r - \langle r\rangle)^2\rangle$, are calculated and paired with the respective energy conductivity, G, computed for the trajectory. Almost all data computed for polar contacts correspond to hydrogen bonds, and we refer to them interchangeably. Side-chain groups of opposite charge, such as $-\mathrm{NH_3}^+$ and COO^-, are classified as charged contacts. For polar and charged contacts, we introduce a threshold of 1 (kcal mol^{-1})^2/ps to reduce noise in data.

Nonpolar contacts were evaluated if the average minimum distance, $\langle r\rangle$, calculated between the two side chains was less than 5.0 Å, in which case the variance in the distance, $\langle\delta r^2\rangle = \langle(r - \langle r\rangle)^2\rangle$, was computed. If, e.g., two phenylalanines met the average minimum distance between the side chains during 99% of the trajectory, we compared the inverse variance of their minimum distances over time and G. In addition, for nonpolar contacts, a low energy current threshold of 0.05 (kcal mol^{-1})^2/ps was applied to reduce noise in the data. The residues that fall in this regime are Phe, Val, and Leu for HP36, resulting in a total of 7 van der Waals contacts. Values of G and dynamics for all contacts meeting the criteria were evaluated for each NVE simulation and collated. It is possible that some of these residue pairs could be positioned to form hydrogen bonds via backbone interactions. This occurred for one such pair, Phe7−Phe11, which is classified as a backbone−backbone hydrogen bond.

The expectation that G and $\langle\delta r^2\rangle^{-1}$ are proportional, using harmonic oscillator models, has been detailed previously.[11,21] A master equation for energy transfer between residue pairs in the protein, $\mathrm{d}E_A/\mathrm{d}t = \sum_{A'\neq A} w_{AA'}E_{A'} - w_{A'A}E_A$, where E_A is the energy of residue A and $w_{AA'}$ a rate constant between A and A', proportional to G, has a form that is similar to the equation of motion for lattice vibrations, $m_A(\mathrm{d}^2u_A/\mathrm{d}t^2) = \sum_{A'\neq A} f_{AA'}u_{A'}$, where m_A and u_A are the mass and displacement, respectively, at site A and $f_{AA'}$ is the force constant. The equations differ by the presence of first and second order time derivatives in the master equation and the equation of motion for lattice vibrations, respectively, and some solutions to the master equation can be obtained from solutions to the vibrational dynamics by substituting t for ω^{-2}.[68−71] The interchangeability of ω^2 and t^{-1} has been found in previous computational studies of vibrational dynamics and energy flow in proteins.[13,72−74] For an oscillator $\omega^2 \propto \langle\delta r^2\rangle^{-1}$, so that for a rate, $G \propto \langle\delta r^2\rangle^{-1}$ after making the ω^2 to t^{-1} substitution. Larger force constants are associated with higher frequencies and faster rates, and we expect energy transfer across polar contacts to be faster than that across nonpolar contacts. Nevertheless, oscillations of different polar contacts may lie in different spectral regions, so that, while $G \propto \langle\delta r^2\rangle^{-1}$ for a contact, different polar contacts may exhibit different linear relations, as has been observed,[11,21,23] and will be further discussed here.

A different approach demonstrating that the rate of energy transfer across a contact is proportional to $\langle\delta r^2\rangle^{-1}$ by Stock and co-workers[22] considers a spring connecting each atom forming the contact, which in turn interacts with the rest of the protein by a pair of springs, one on each side of each atom forming the contact. Taking the latter spring constants to have the same value, they find that not only is the rate of energy transfer across the contact proportional to $\langle\delta r^2\rangle^{-1}$ but also the constant of proportionality becomes smaller with increasing strength of the spring constant between the atoms forming the contact and the rest of the protein. This derivation shows clearly how different contacts may exhibit different linear relations. Both perspectives are based on harmonic oscillator pictures. It may thus be not all that surprising that a proportionality between the rate constant for energy transfer and $\langle \delta r^2 \rangle^{-1}$ was observed based on the results of MD simulations carried out at very low temperature,[20] at which the protein structure was restricted and the amplitude of oscillation was relatively small. We do not expect protein dynamics to be harmonic at room temperature, and values of G and $\langle \delta r^2 \rangle^{-1}$ computed from the MD simulations incorporate the full anharmonicity. They serve as a check as to whether or not we can conclude that G and $\langle \delta r^2 \rangle^{-1}$ are indeed proportional at room temperature.

3. RESULTS AND DISCUSSION

We examine the relationship between the energy conductivity, G, and dynamics of nonpolar, van der Waals (vdW) contacts and polar contacts, with particular emphasis on vdW interactions, since no study has yet explored this relation for vdW contacts in proteins near room temperature. For consistency and to compare with earlier work, we also examine the relation between G and contact dynamics of polar contacts of HP36. In previous work, we have neglected hydrogen bonds along α-helices, since rates of energy transport along α-helices exhibit trends seen for energy transport along the main chain,[20] and is affected little by the hydrogen bonds along the helix. Nevertheless, determining a relation between G and contact dynamics for all polar bonds is worthwhile, and the results for α-helices can be compared to energy transfer across other hydrogen bonds to determine any distinct characteristics, which we address here.

Consider first vdW contacts. Five of the seven nonpolar contacts are side chain−side chain and the remaining two are backbone−side chain interactions, as detailed in the Supporting Information. The results are plotted in Figure 1, along with a linear fit to the data. The data plotted in Figure 1a are binned for clarity (bin length of 330 nm^{-2}, approximately 30 points per window); the raw data are plotted in Figure S1 of the Supporting Information. The linear fit to the data plotted in Figure 1a is $G = 0.001967\langle \delta r^2 \rangle^{-1} + 0.6023$, where G is in units of (kcal mol^{-1})^2 ps^{-1} and $\langle \delta r^2 \rangle^{-1}$ in nm^{-2}; the R^2 value for the linear fit is 0.95. Figure 1b depicts the location of these nonpolar contacts, which are listed in Table S1 of the Supporting Information. Though the data are formed from seven contact pairs, they appear to exhibit a single linear variation between G and $\langle \delta r^2 \rangle^{-1}$.

Of the vdW contacts investigated, Phe11−Leu29 has the largest values of G and smallest $\langle \delta r^2 \rangle$. Figure S1 depicts the raw data for this pair as green triangles. For this contact, there is a relatively strong interaction between the phenyl ring of Phe11 and the isopropyl group of Leu29. A subset of the time, the alpha hydrogen of Leu also interacts with the phenyl ring; however, the effect of this latter interaction is very small when we compare values of G when it is present and when it is absent. Overall, the relatively large values of G compared to other nonpolar contacts are due to the multiple atomic interactions between these side chains, which also contribute to the relatively large values of $\langle \delta r^2 \rangle^{-1}$. When those values are particularly large, generally, multiple atomic interactions exist during the simulation; in contrast, lower values of $\langle \delta r^2 \rangle^{-1}$ as well as G are associated with single atomic interactions. Other noteworthy vdW contacts include interactions between phenyl side chains. There are two such interactions, shown in blue in Figure S1. These interactions generally have somewhat smaller G than the other vdW interactions.

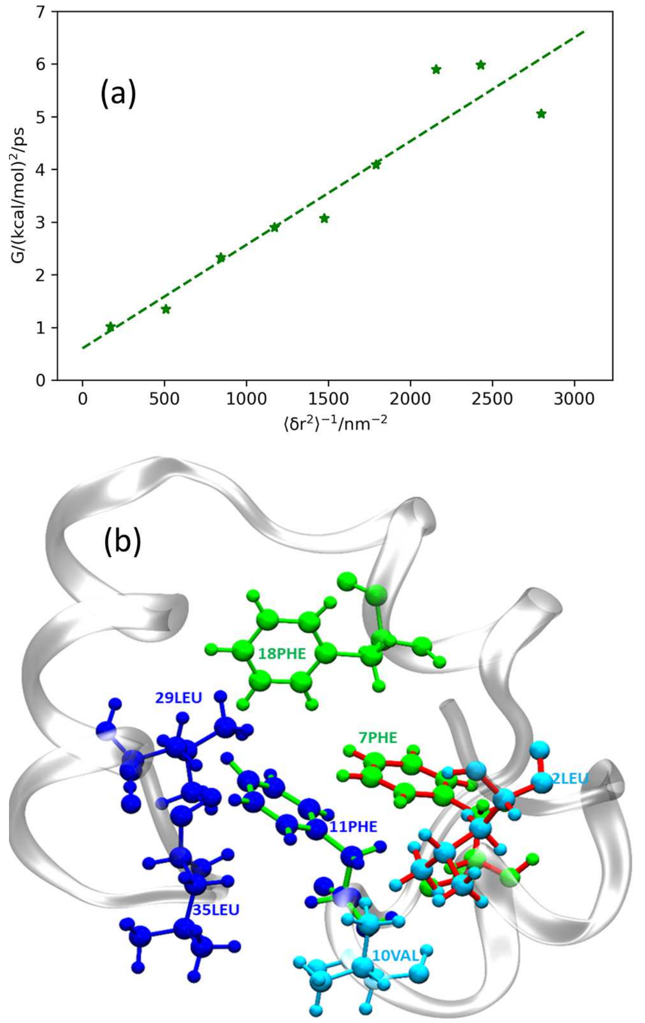

Figure 1. (a) Plot of energy conductivity, G, as a function of the inverse of the variance in contact length, $\langle \delta r^2 \rangle^{-1}$, for van der Waals (vdW) contacts. The vdW contacts include Leu2−Phe7, Leu2−Val10, Phe7−Phe18, Phe11−Phe18, Phe11−Leu29, Phe11−Leu35, and Leu29−Leu35. A linear fit to the data (R^2 value 0.95), specified in the main text, is also plotted. (b) The HP36 residues involved in vdW interactions, where each contact shares the same color. Residues involved in multiple contacts are rendered with different colors for the bonds and atoms; e.g., there exists a contact pair if either bonds or atoms share the same color.

We turn now to polar contacts, which, as we will see, exhibit values of G that are 1−2 orders of magnitude larger than those for vdW contacts. Polar contact G values rise above noise levels produced in the computational analysis much more frequently than those of vdW contacts, which is why they have been studied in previous work on larger proteins. Here, as noted above, we include for the first time hydrogen bonds of α-helices, which we refer to as helical contacts. They form the majority of hydrogen bonds of HP36. In Figure 2, we plot G versus $\langle \delta r^2 \rangle^{-1}$ for helical contacts, where the raw data (Figure S2) was binned applying a window size of 372 nm^{-1}, approximately 53 points per window. The linear fit to the data is $G = 0.019\langle \delta r^2 \rangle^{-1} + 9.49$, where G is in units of (kcal mol^{-1})^2 ps^{-1} and $\langle \delta r^2 \rangle^{-1}$ in nm^{-2} (R^2 value of 0.96). Residue pairs of helical contacts are depicted in Figure 3 in magenta,

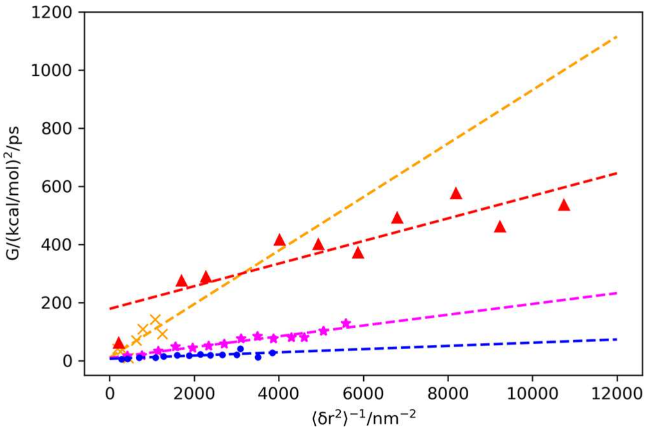

Figure 2. Values of G for polar contacts as a function of the inverse of the variance, $\langle \delta r^2 \rangle^{-1}$, in the distances of the contact. The data plotted in blue correspond to Lys30−Leu35, Phe7−Met13, and Ala19−Gln26. The data plotted in magenta correspond to helical contacts. The points plotted in orange consist of data from contacts of Phe18−Gln26, Leu21−Gln26, and Lys30−Phe36. Charged contacts appear as red triangles and correspond to interactions between Leu2−Arg15, Asp4−Arg15, and Val10−Lys33.

and a full list of the contacts including the hydrogen bond distance and angle criteria that each contact meets over the simulation time appears in Table S2.

It is interesting to compare the relative time helical contacts stay intact compared to other hydrogen bonds, which are listed in Table S3 and discussed further below. We see, as expected, that contacts located along the helices are more stable than those in the loop region. In the former case, the hydrogen bonds remain intact, including distance and angle criteria, for about 60% of the full (100 ns NPT) simulation time, while those of other regions remain intact for about 20% of the full simulation. We note that we only calculate G during times when the contact remains intact. Furthermore, the helical contacts sample a greater range of $\langle \delta r^2 \rangle^{-1}$ than the other contacts plotted in Figure 2, consistent with greater structural rigidity of the helices. One pair, Phe7−Phe11, two residues that form part of the core of the protein, interacts via both vdW contacts through the side chains as well as a hydrogen bond through the backbone, specifically via a backbone hydrogen bond for 75% of the full simulation time and for some of that time the phenyl rings are in contact providing a second pathway for energy transfer. This may explain why values of G for Phe7−Phe11 are higher on average than all other backbone contacts with hydrogen bonds.

Results for polar contacts with lower average G for a given $\langle \delta r^2 \rangle^{-1}$ are plotted in blue in Figure 2, and residues forming those contacts are indicated in blue in Figure 3. These contacts include Lys30−Leu35, Phe7−Met13, and Ala19−Gln26. For clarity, the data has been binned using a window size of 256 nm^{-1} with approximately 13 points per window. (The full data appear in Figure S2.) The linear fit to the data is $G = 0.0048\langle \delta r^2 \rangle^{-1} + 7.27$, with the same units as those for the other fits. Though the data appear to fit well to the linear fit, the value of R^2, 0.77, is smaller than that for the helical contacts, perhaps because of the much smaller values of G, which fluctuate close to the noise threshold. These contacts, which have comparatively lower values of G, also exhibit the lowest contact proportion over the 100 ns NPT simulation (Table S3), far smaller than that for the helical contacts, noted above.

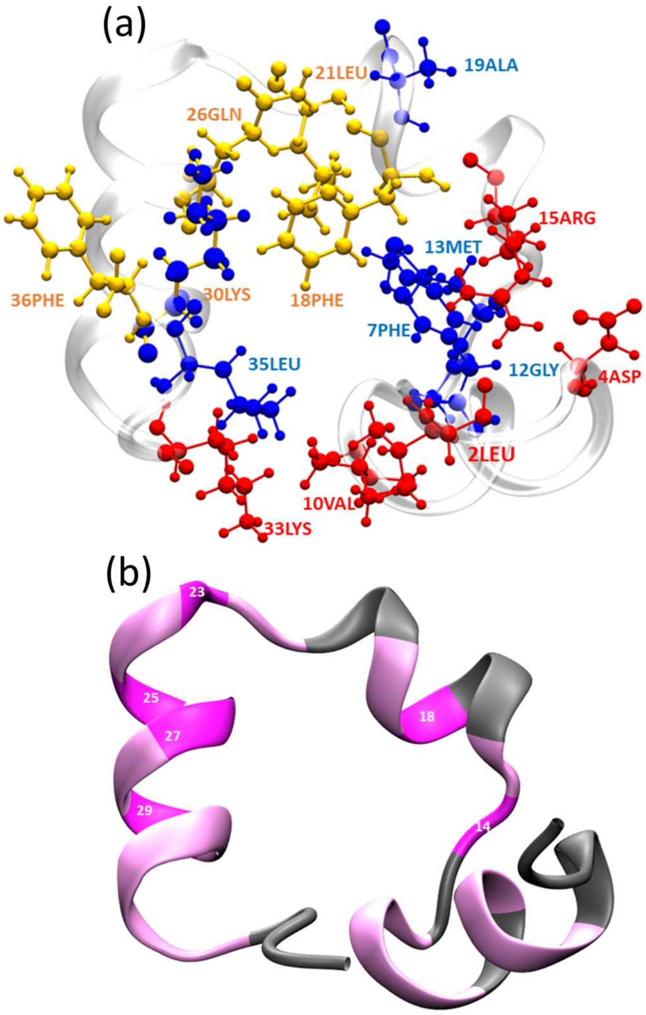

Figure 3. (a) The residues shown in orange and blue correspond to the orange and blue curves of the polar contacts in Figure 2, while the residues colored in red are the charged contacts, corresponding to data plotted in Figure 2. If a residue falls into two regimes, bond and atom spheres are colored distinctly corresponding to its pairs. (b) The contacts involved in the formation of backbone−backbone hydrogen bonds are shown in magenta. Hydrogen bonds lasting more than 80% of the total simulation (100 ns NPT) time are colored darker, while those intact for between 60 and 80% are more faded magenta. All contact times are listed in Table S2.

We observe special cases where the trend of G vs $\langle \delta r^2 \rangle^{-1}$ exhibits a relatively large slope. Results for the contacts Phe18−Gln26, Leu21−Gln26, and Lys30−Phe36 are plotted in orange in Figures 2 and 3. It is interesting to note that in prior studies the contact pair Phe18−Gln26 exhibited a relatively large rate of energy transfer, based both on computing the local energy diffusivity[51−54] for this pair as well as fitting the results of all-atom nonequilibrium MD simulations to a master equation form.[19,20] For these polar contacts, with relatively large G for a given $\langle \delta r^2 \rangle^{-1}$, depicted in orange, the linear fit to the computed results is $G = 0.09\langle \delta r^2 \rangle^{-1} + 10.4$, with the same units as those for the other fits and with an R^2 value of 0.79. The data were binned for clarity using a window size of 156 nm^{-1} where there are approximately 18.75 points per window.

We consider now charged contacts, which we take to include residue contacts involving two charged side chains containing, e.g., $-NH_3^+$ and $-COO^-$. In a previous study of interactions

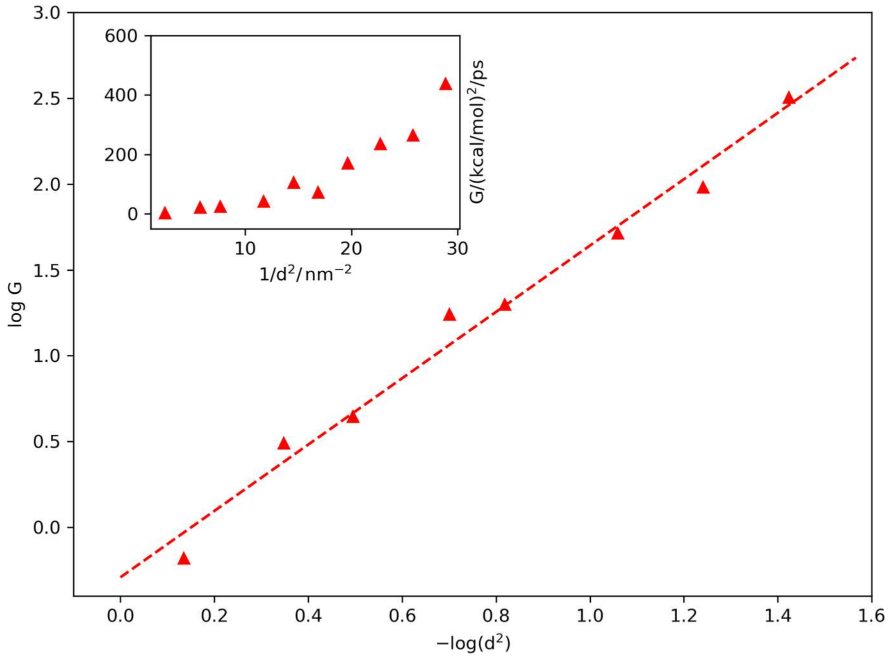

Figure 4. Log−log plot of G vs the inverse of the mean square distance, d^2, between charged contacts. The inset plots G vs the inverse of the mean square distance of that contact. The line includes the contacts Leu2−Arg15, Asp4−Arg15, and Val10−Lys33, which are highlighted in red in Figure 3a.

between charged contacts of myoglobin, we found a plot of G vs $\langle \delta r^2 \rangle^{-1}$ did not exhibit a linear relation when the length of the contact was small.[21] Unlike hydrogen bonds, which are defined only at short range, charged groups interact over longer distances. The breakdown of a linear relation that was seen for the charged contacts of myoglobin is probably due to simultaneous and comparable interactions of charged groups on more than two nearby residues in this protein.[21]

For HP36, we analyze the charged contacts Leu2−Arg15, Asp4−Arg15, and Val10−Lys33, shown in red in Figure 3a. We consider first G against the inverse of variance in the contact distance, $\langle \delta r^2 \rangle^{-1}$, when the charged groups are in close contact. The data, binned for clarity using a window size of 916 nm^{-1} with approximately 12.5 points per window, are plotted in Figure 2 as red points. A linear fit to the data yields $G = 0.0398 + 177.39$, where units are the same as those in previous linear fits. The R^2 value of the linear fit is 0.89. The variation of G and $\langle \delta r^2 \rangle^{-1}$ that we find for the charged contacts of HP36 appears rather linear, particularly at large $\langle \delta r^2 \rangle^{-1}$ much more so than we found in a previous analysis of charged contacts of myoglobin. That may be due to the smaller number of charged contacts in HP36, which diminishes the chance of mutual interactions between more than two residues. For myoglobin,[21] we found a diffusion equation fit the data for charged contacts, and we consider that here, too.

In keeping with a diffusion picture for energy transport, we examine a relation between G and the mean square distance, $d^2 \equiv \langle r^2 \rangle$, between the charged atoms of a residue pair,

$$G \propto (d^2)^{-b} \tag{4}$$

For normal diffusion, $b = 1$, but in general, other power law variations are possible.[21] The plot of $\log(G)$ against $-\log(d^2)$ for charged contacts, where the data has been binned for clarity using an equidistant window of 0.13 in units of $-\log(d^2)$, approximately 12.5 points per window, is shown in Figure 4. (The raw data appear in Figures S4 and S5.) The linear fit to the data is $\log(G) = -1.93 \log(d^2) + 0.30$, with an R^2 value of 0.99. We thus find $b \approx 1.9$; as for myoglobin,[21] b can be greater than 1 when there are multiple charges interacting between residue pairs, as there are for Leu2−Arg15 and Asp4−Arg15, which comprise most of the data and span the full region in $\log(G)$ and $-\log(d^2)$ (see Figure S4). Contributions of individual contacts to the variation of G with $1/d^2$ and $\log(G)$ with $-\log(d^2)$ are plotted in Figures S4 and S5, respectively. The individual data deviate far less from the overall trends than is the case for G vs $\langle \delta r^2 \rangle^{-1}$ (Figure S3). While the linear relation between G vs $\langle \delta r^2 \rangle^{-1}$ is supported by the data, particularly at larger $\langle \delta r^2 \rangle^{-1}$, there appears to be a clearer relationship between G and $1/d^2$ for contacts that exhibit larger G.

It is of interest to compare trends in the results of G computed for residue pairs of HP36 in this study with the local energy diffusivity computed in previous work.[19] Both of these quantities are proportional to the rate of energy transfer between residue pairs. We compare their relative values, though computed with two different methods and different force fields, to examine the consistency of the methods used. In Figure 5, we provide a map of values of G, which can be compared with an analogous map plotted as Figure 3 in ref 19. The latter was computed using a single structure, whereas for Figure 5 we have averaged values of G obtained from all of the 50 NVE simulations, where each NVE simulation was allowed to evolve for a total of 500 ps. Only an average G of at least 0.2 $(\text{kcal mol}^{-1})^2\ \text{ps}^{-1}$ for a residue pair is indicated in Figure 5.

The results for all nonbonded contacts with relatively large G are consistent with residue pairs with relatively large local energy diffusivity reported in ref 19. There are some differences seen upon a detailed comparison, two of which are noteworthy. In both studies, the rate of energy transfer between Val10 and Lys33 and Phe11 and Lys33 are large, but in the previous study, it was greater for Phe11−Lys33 than for Val10−Lys33, whereas this is reversed in our study. In

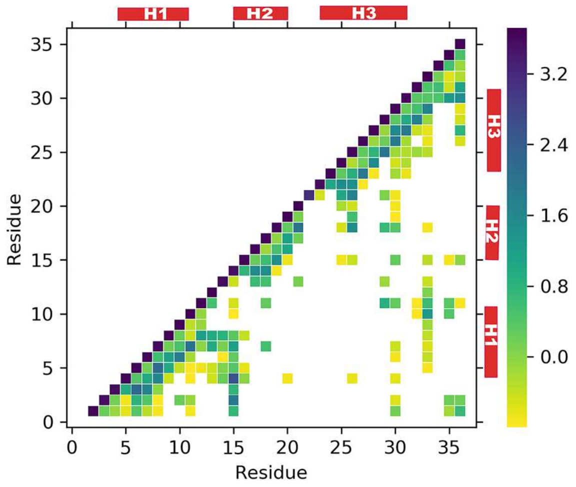

Figure 5. A map of G values between residue pairs for HP36. The contacts for which $G \geq 0.2$ (kcal/mol)^2/ps, out of 50 NVE simulations, are selected in the plot. Values of G are converted to a log scale, and the range is shown in the color bar. The three helices of HP36 are labeled above as H1, H2, and H3.

addition, the contact Leu2−Arg15 exhibits a large G in this study, which can be identified easily as dark blue in Figure 5, whereas the relative rate was significantly smaller in ref 19. The relative rates of energy transfer between other contacts are in good agreement with those found in ref 19. The contacts Asp4−Arg15 and Phe18−Gln26, the role of which in energy transport was emphasized in the earlier study,[19] also exhibit relatively large values of G in this study.

Recently, Stock and co-workers have further examined the relation between equilibrium fluctuations and rate constants of a master equation.[22] They simulated energy transport in a number of proteins at 300 K including HP36. They fit results of all-atom nonequilibrium MD simulations to a master equation and found the rate constants for energy transfer across the contacts Asp4−Arg15 and Phe18−Gln26 to be largest. For those two, they analyzed the scaling of the rate constant with variance in the distance of the contact and found each fits reasonably well along one of two linear relations that are comprised of rate constants obtained for all of the proteins of their study.

We can relate the values of G that we have computed to rate constants as described in section 2, beginning with the conversion $w \approx G/[1180\ (\text{kcal mol}^{-1})^2]$ presented there. With this conversion, we estimate for the rate constant for energy transfer across the Asp4−Arg15 contact a value of about 0.3 ps^{-1}, which is about a factor of 2−3 larger than the rate constant obtained from the fit to the master equation in ref 22. The conversion incorporates the average number of degrees of freedom of an amino acid. Asp4−Arg15 has 126 degrees of freedom, so for this pair, the conversion becomes $w \approx G/[1412\ (\text{kcal mol}^{-1})^2]$ and the rate constant 0.25 ps^{-1}, about a factor of 2 larger than the rate constant obtained in ref 22. For Phe18−Gln26, we estimate using the generic conversion provided in section 2, $w \approx G/[1180\ (\text{kcal mol}^{-1})^2]$, a rate constant of 0.03 ps^{-1}, about a factor of 1.5 smaller than the rate constant obtained from the fit to the master equation in ref 22. Phe18−Gln26 has 129 degrees of freedom, so that the conversion for this pair becomes $w \approx G/[1480\ (\text{kcal mol}^{-1})^2]$, and the rate constant 0.025 ps^{-1}, about a factor of 2 smaller than the rate constant obtained in ref 22. We present these values just as a reference, since the approaches and force field models used are different, and the counterions included in our MD simulations will affect values of G, but overall, the results agree reasonably well.

One conclusion of ref 22, in agreement with our own analysis, is that there is generally a better fit for a relation between the rate constant and $1/d^2$ for contacts with relatively large G or rate constant. As discussed above, $1/d^2$ provides a good predictor of G for contacts with relatively large G. However, for individual contacts, the established linear relation G vs $\langle \delta r^2 \rangle^{-1}$ is useful, as it allows from measurements of rates of energy transfer the determination of changes in dynamics, and entropy associated with the dynamics, with change in functional state or mutation. Evidence for the proportionality between G and $\langle \delta r^2 \rangle^{-1}$ for vdW contacts provided here is particularly useful, since ultrafast time-resolved measurements have been carried out to detect energy transfer across vdW contacts.[4] A relation between energy transfer and contact dynamics can also be applied to study relaxation processes and changes in the flexibility of contacts in intrinsically disordered protein (IDP) systems.[75]

As pointed out previously, for a change in functional state, the change in entropy, ΔS, associated with changes in contact dynamics can be estimated by measuring a change in G.[11,21] Suppose, e.g., that a protein changes state from unliganded (U) to liganded (L). For $\Delta S = S_L - S_U$, where S_L (S_U) refers to the entropy associated with the dynamics of a particular contact pair in the liganded (unliganded) state, the proportionality between G and $\langle \delta r^2 \rangle^{-1}$ means that[11,21] $\Delta S = \frac{k_B}{2} \ln\left(\frac{G_U}{G_L}\right) = \frac{k_B}{2} \ln\left(\frac{\langle \delta r^2 \rangle_L}{\langle \delta r^2 \rangle_U}\right)$. Therefore, measurement of the rate of energy transfer in each state can provide information about the change in dynamics of the contact across which energy transfer occurs and the entropy associated with the dynamics. This change can also be determined when a mutation is introduced. In one study of myoglobin mutants,[24] e.g., no change in the rate of energy transfer across a vdW contact was measured, consistent with a contact that remains unchanged for the mutations studied, as was seen in results of molecular simulations of the mutants.

4. CONCLUSIONS

Recent studies of energy transfer across hydrogen bonds between protein residues and between amino acids and water have identified relations between the rate of energy transfer and fluctuations in the length of the hydrogen bond.[11,21−23] Specifically, the rate of energy transfer is proportional to the inverse of the variance in the length of the bond, computed at equilibrium. Earlier work on energy transport in HP36 at low temperature indicated that such a proportionality holds not only for hydrogen bonds but also for nonpolar contacts.[20] In this study, we find the scaling of rates of energy transfer with the inverse of the variance in the contact length holds up well for van der Waals contacts around room temperature. We have also examined hydrogen bonds that stabilize α-helices, which in prior work had been neglected. The proportionality between the rate of energy transfer across hydrogen bonds of α-helices and the inverse of the variance in their length also holds up well at 300 K, with a constant of proportionality that is different than that for other hydrogen bonds that we have studied thus far.

We find the rates of energy transfer across van der Waals contacts of HP36 to be 1 or 2 orders of magnitude slower than the rates of energy transfer across polar contacts.[20] In this respect, energy transport through this protein is determined more by the backbone and polar contacts than by nonpolar interactions. It may even be possible in some cases to model energy transport through proteins by neglecting the contribution of van der Waals contacts altogether.[22] However, rates of energy transfer across van der Waals contacts have been measured in a number of time-resolved experiments,[4,5,24−27] motivating our study of the relation between energy transfer rates and equilibrium dynamics of van der Waals contacts at temperatures around 300 K. For example, time-resolved Raman experiments of energy transfer in mutants of myoglobin, where energy flow into and out of tryptophans is monitored, have provided a picture of anisotropic energy transport in this protein, a role played by van der Waals contacts in this process and effects of mutation.[4,15]

Because the rate of energy transfer is related to the dynamics of the contact, measurements of energy transfer across van der Waals contacts not only provide information about the rate and direction of energy transport following photoexcitation of a protein or following a chemical reaction but also can be interpreted in terms of the underlying dynamics of contacts. If there is a change in that rate due to a change in the functional state of the protein, or due to mutation, corresponding changes in the dynamics of the contact, and in the entropy associated with the dynamics, can be determined by time-resolved spectroscopic measurements of the rates. Mutations that leave the contacts in place, with little effect on the dynamics of the contact, will likely not affect energy transfer across the contact, as has been observed experimentally.[24]

Though individual contact pairs may exhibit a linear variation between rates of energy transfer and the inverse of the variance in the length of the contact at equilibrium, different sets of contacts may exhibit a different constant of proportionality, as we have seen for hydrogen bonds. While for HP36 all van der Waals contacts exhibited the same trend in the rate of energy transfer with contact dynamics, that may not generally hold for other proteins, which will require further study. While rates of energy transfer across van der Waals contacts in HP36 are relatively small, compared to energy transfer across polar contacts and within the main chain, rates of energy transfer across van der Waals contacts on the scale of ps^{-1} have been measured for other systems.[24]

Beyond biomolecules, a more detailed understanding of the relation between energy transfer across van der Waals contacts and contact dynamics would also provide useful information about the influence of contacts in thermal transport across molecular junctions and interfaces.[11,76−86] Thermal transport across molecular junctions at room temperature appears only modestly impeded when covalent contacts between the molecules and leads are replaced by van der Waals contacts, despite the large change in interaction between the molecule and the substrate.[86] The relatively small effect on the thermal conductance of the junction may be due to a combination of restricted contact dynamics and to the wavelength of phonons that transport heat in the junction. Energy transfer across van der Waals contacts in proteins may likewise depend on the protein vibrations that transport energy, a relationship that requires further study.

■ ASSOCIATED CONTENT

Supporting Information

The Supporting Information is available free of charge at https://pubs.acs.org/doi/10.1021/acs.jpcb.0c08091.

> Scaling figures identifying specific residue pairs with a complete set of data points, tables listing residue pairs, and a list of residues of HP36 (PDF)

■ AUTHOR INFORMATION

Corresponding Author

David M. Leitner − *Department of Chemistry, University of Nevada, Reno, Nevada 89557, United States;* orcid.org/0000-0002-3105-818X; Email: dml@unr.edu

Authors

Humanath Poudel − *Department of Chemistry, University of Nevada, Reno, Nevada 89557, United States*

Korey M. Reid − *Department of Chemistry, University of Nevada, Reno, Nevada 89557, United States*

Takahisa Yamato − *Graduate School of Science, Division of Material Science, Nagoya University, Nagoya 464-8602, Japan;* orcid.org/0000-0002-0685-861X

Complete contact information is available at: https://pubs.acs.org/10.1021/acs.jpcb.0c08091

Notes

The authors declare no competing financial interest.

■ ACKNOWLEDGMENTS

Part of this work was carried out while D.M.L. was a JSPS Invitational Fellow at Nagoya University. Support from NSF Grant CHE-1854271 (D.M.L.) is gratefully acknowledged.

■ REFERENCES

(1) Leitner, D. M.; Straub, J. E. *Proteins: Energy, Heat and Signal Flow*; CRC Press, Taylor & Francis Group: Boca Raton, FL, 2010.

(2) Leitner, D. M.; Yamato, T. Recent Developments in the Computational Study of Protein Structural and Vibrational Energy Dynamics. *Biophys. Rev.* **2020**, *12*, 317−322.

(3) Leitner, D. M.; Yamato, T. Mapping Energy Transport Networks in Proteins. *Rev. Comput. Chem.* **2018**, *31*, 63−114.

(4) Mizuno, M.; Mizutani, Y. Role of Atomic Contacts in Vibrational Energy Transfer in Myoglobin. *Biophys. Rev.* **2020**, *12*, 511−518.

(5) Baumann, T.; Hauf, M.; Schildhauer, F.; Eberl, K. B.; Durkin, P. M.; Deniz, E.; Löffler, J. G.; Acevedo-Rocha, C. G.; Jaric, J.; Martins, B. M.; et al. Observation of Site-Resolved Vibrational Energy Transfer Using a Genetically Encoded Ultrafast Heater. *Angew. Chem., Int. Ed.* **2019**, *58*, 2899−2903.

(6) Levantino, M.; Schiro, G.; Lemke, H. T.; Cottone, G.; Glownia, J. M.; Zhu, D.; Chollet, M.; Ihee, H.; Cupane, A.; Cammarata, M. Ultrafast Myoglobin Structural Dynamics Observed with an X-Ray Free-Electron Laser. *Nat. Commun.* **2015**, *6*, 6772.

(7) Barends, T. R. M.; Foucar, L.; Ardevol, A.; Nass, K.; Aquila, A.; Botha, S.; Doak, R. B.; Falahati, K.; Hartmann, E.; Hilpert, M.; et al. Direct Observation of Ultrafast Collective Motions in CO Myoglobin Upon Ligand Dissociation. *Science* **2015**, *350*, 445−450.

(8) Gulzar, A.; Valino-Borau, L.; Buchenberg, S.; Wolf, S.; Stock, G. Energy Transport Pathways in Proteins: A Nonequilibrium Molecular Dynamics Simulation Study. *J. Chem. Theory Comput.* **2019**, *15*, 5750−5757.

(9) Ota, K.; Yamato, T. Energy Exchange Network Model Demonstrates Protein Allosteric Transition: An Application to an Oxygen Sensor Protein. *J. Phys. Chem. B* **2019**, *123*, 768−775.

(10) Brinkmann, L. U. L.; Hub, J. S. Ultrafast Anisotropic Protein Quake Propagation after CO Photodissociation in Myoglobin. *Proc. Natl. Acad. Sci. U. S. A.* **2016**, *113*, 10565−10570.

(11) Leitner, D. M.; Pandey, H. D.; Reid, K. M. Energy Transport across Interfaces in Biomolecular Systems. *J. Phys. Chem. B* **2019**, *123*, 9507−9524.

(12) Agbo, J. K.; Xu, Y.; Zhang, P.; Straub, J. E.; Leitner, D. M. Vibrational Energy Flow across Heme-Cytochrome c and Cytochrome c-Water Interfaces. *Theor. Chem. Acc.* **2014**, *133*, art. no. 1504. DOI: 10.1007/s00214-014-1504-7

(13) Leitner, D. M. Energy Flow in Proteins. *Annu. Rev. Phys. Chem.* **2008**, *59*, 233−259.

(14) Martínez, L.; Figueira, A. C. M.; Webb, P.; Polikarpov, I.; Skaf, M. S. Mapping the Intramolecular Vibrational Energy Flow in Proteins Reveals Functionally Important Residues. *J. Phys. Chem. Lett.* **2011**, *2*, 2073−2078.

(15) Mizutani, Y. Time-Resolved Resonance Raman Spectroscopy and Application to Studies on Ultrafast Protein Dynamics. *Bull. Chem. Soc. Jpn.* **2017**, *90*, 1344−1371.

(16) Yang, C.; Choi, M.; Kim, J. G.; Kim, H.; Muniyappan, S.; Nozawa, S.; Adachi, S.; Henning, R.; Kosheleva, I.; Ihee, H. Protein Structural Dynamics of Wild-Type and Mutant Homodimeric Hemoglobin Studied by Time-Resolved X-Ray Solution Scattering. *Int. J. Mol. Sci.* **2018**, *19*, 3633.

(17) Nguyen, P. H.; Hamm, P.; Stock, G. Nonequilibrium Molecular Dynamics Simulation of Photoinduced Energy Flow in Peptides: Theory Meets Experiment. In *Proteins: Energy, Heat and Signal Flow*; Leitner, D. M., Straub, J. E., Eds.; CRC Press, Taylor & Francis Group: Boca Raton, FL, 2010; pp 149−168.

(18) Hoang Viet, M.; Derreumaux, P.; Li, M. S.; Roland, C.; Sagui, C.; Nguyen, P. H. Picosecond Dissociation of Amyloid Fibrils with Infrared Laser: A Nonequilibrium Simulation Study. *J. Chem. Phys.* **2015**, *143*, 155101.

(19) Leitner, D. M.; Buchenberg, S.; Brettel, P.; Stock, G. Vibrational Energy Flow in the Villin Headpiece Subdomain: Master Equation Simulations. *J. Chem. Phys.* **2015**, *142*, 075101.

(20) Buchenberg, S.; Leitner, D. M.; Stock, G. Scaling Rules for Vibrational Energy Transport in Proteins. *J. Phys. Chem. Lett.* **2016**, *7*, 25−30.

(21) Reid, K. M.; Yamato, T.; Leitner, D. M. Scaling of Rates of Vibrational Energy Transfer in Proteins with Equilibrium Dynamics and Entropy. *J. Phys. Chem. B* **2018**, *122*, 9331−9339.

(22) Valino-Borau, L.; Gulzar, A.; Stock, G. Master Equation Model to Predict Energy Transport Pathways in Proteins. *J. Chem. Phys.* **2020**, *152*, 045103.

(23) Reid, K. M.; Yamato, T.; Leitner, D. M. Variation of Energy Transfer Rates across Protein−Water Contacts with Equilibrium Structural Fluctuations of a Homodimeric Hemoglobin. *J. Phys. Chem. B* **2020**, *124*, 1148−1159.

(24) Yamashita, S.; Mizuno, M.; Tran, D. P.; Dokainish, H.; Kitao, A.; Mizutani, Y. Vibrational Energy Transfer from Heme through Atomic Contacts in Proteins. *J. Phys. Chem. B* **2018**, *122*, 5877−5884.

(25) Kondoh, M.; Mizuno, M.; Mizutani, Y. Importance of Atomic Contacts in Vibrational Energy Flow in Proteins. *J. Phys. Chem. Lett.* **2016**, *7*, 1950−1954.

(26) Fujii, N.; Mizuno, M.; Mizutani, Y. Direct Observation of Vibrational Energy Flow in Cytochrome C. *J. Phys. Chem. B* **2011**, *115*, 13057−64.

(27) Fujii, N.; Mizuno, M.; Ishikawa, H.; Mizutani, Y. Observing Vibrational Energy Flow in a Protein with the Spatial Resolution of a Single Amino Acid Residue. *J. Phys. Chem. Lett.* **2014**, *5*, 3269−3273.

(28) Henry, E. R.; Eaton, W. A.; Hochstrasser, R. M. Molecular Dynamics Simulations of Cooling in Laser-Excited Heme Proteins. *Proc. Natl. Acad. Sci. U. S. A.* **1986**, *83*, 8982−8986.

(29) Mizutani, Y.; Kitagawa, T. Direct Observation of Cooling of Heme Upon Photodissociation of Carbonmonoxy Myoglobin. *Science* **1997**, *278*, 443−446.

(30) Lian, T.; Locke, B.; Kholodenko, Y.; Hochstrasser, R. M. Energy Flow from Solute to Solvent Probed by Femtosecond Ir Spectroscopy: Malachite Green and Heme Protein Solutions. *J. Phys. Chem.* **1994**, *98*, 11648−11656.

(31) Sagnella, D. E.; Straub, J. E.; Jackson, T. A.; Lim, M.; Anfinrud, P. A. Vibrational Population Relaxation of Carbon Monoxide in the Heme Pocket of Carbonmonoxy Myoglobin: Comparison of Time-Resolved Mid-IR Absorbance Experiments and Molecular Dynamics Simulations. *Proc. Natl. Acad. Sci. U. S. A.* **1999**, *96*, 14324−14329.

(32) Nagy, A. M.; Raicu, V.; Miller, R. J. D. Nonlinear Optical Studies of Heme Protein Dynamics: Implications for Proteins as Hybrid States of Matter. *Biochim. Biophys. Acta, Proteins Proteomics* **2005**, *1749*, 148−172.

(33) Tanimura, Y. Numerically "Exact" Approach to Open Quantum Dynamics: The Hierarchical Equations of Motion (HEOM). *J. Chem. Phys.* **2020**, *153*, 020901.

(34) Ishizaki, A.; Tanimura, Y. Modeling Vibrational Dephasing and Energy Relaxation of Intramolecular Anharmonic Modes for Multidimensional Infrared Spectroscopies. *J. Chem. Phys.* **2006**, *125*, 084501.

(35) Tanimura, Y. Stochastic Liouville, Langevin, Fokker−Planck, and Master Equation Approaches to Quantum Dissipative Systems. *J. Phys. Soc. Jpn.* **2006**, *75*, 082001.

(36) Tanimura, Y.; Kubo, R. Time Evolution of a Quantum System in Contact with a Nearly Gaussian-Markoffian Noise Bath. *J. Phys. Soc. Jpn.* **1989**, *58*, 101−114.

(37) Tanimura, Y.; Wolynes, P. G. Quantum and Classical Fokker-Planck Equations for a Gaussian-Markovian Noise Bath. *Phys. Rev. A: At., Mol., Opt. Phys.* **1991**, *43*, 4131−4142.

(38) Bu, L.; Straub, J. E. Simulating Vibrational Energy Flow in Proteins: Relaxation Rate and Mechanism for Heme Cooling in Cytochrome c. *J. Phys. Chem. B* **2003**, *107*, 12339−12345.

(39) Ishikura, T.; Iwata, Y.; Hatano, T.; Yamato, T. Energy Exchange Network of Inter-Residue Interactions within a Thermally Fluctuating Protein: A Computational Study. *J. Comput. Chem.* **2015**, *36*, 1709−1718.

(40) Ishikura, T.; Yamato, T. Energy Transfer Pathways Relevant for Long-Range Intramolecular Signaling of Photosensory Protein Revealed by Microscopic Energy Conductivity Analysis. *Chem. Phys. Lett.* **2006**, *432*, 533−537.

(41) Maggi, L.; Carloni, P.; Rossetti, G. Vibrational Energy in Proteins Correlates with Tolopogy. *J. Phys. Chem. Lett.* **2018**, *9*, 6393−6398.

(42) Wang, W. B.; Liang, Y.; Zhang, J.; Wu, Y. D.; Du, J. J.; Li, Q. M.; Zhu, J. Z.; Su, J. G. Energy Transport Pathway in Proteins: Insights from Non-Equilibrium Molecular Dynamics with Elastic Network Model. *Sci. Rep.* **2018**, *8*, 9487.

(43) Harder-Viddal, C.; Roshko, R. M.; Stetefeld, J. Energy Flow and Intersubunit Signalling in GSAM: A Non-Equilibrium Molecular Dynamics Study. *Comput. Struct. Biotechnol. J.* **2020**, *18*, 1651−1663.

(44) Nagaoka, M.; Yu, I.; Takayanagi, M., Energy Flow Analysis in Proteins Via Ensemble Molecular Dynamics Simulations: Time-Resolved Vibrational Analysis and Surficial Kirkwood-Buff Theory. In *Proteins: Energy, Heat and Signal Flow*, Leitner, D. M.; Straub, J. E., Eds. Taylor & Francis Group, CRC Press: Boca Raton, 2010; pp 169−196.

(45) Yamato, T. Energy Flow Pathways in Photoreceptor Proteins. In *Proteins: Energy, Heat and Signal Flow*; Leitner, D. M., Straub, J. E., Eds.; CRC Press, Taylor and Francis Group: Boca Raton, FL, 2010; pp 129−147.

(46) Stock, G. Classical Simulation of Quantum Energy Flow in Biomolecules. *Phys. Rev. Lett.* **2009**, *102*, 118301.

(47) Yu, X.; Leitner, D. M. Vibrational Energy Transfer and Heat Conduction in a Protein. *J. Phys. Chem. B* **2003**, *107*, 1698−1707.

(48) Fujisaki, H.; Zhang, Y.; Straub, J. E. Non-Markovian Theory of Vibrational Energy Relaxation and Its Applications to Biomolecular Systems. *Adv. Chem. Phys.* **2011**, *145*, 1−33.

(49) Xu, Y.; Leitner, D. M. Vibrational Energy Flow through the Green Fluorescent Protein-Water Interface: Communication Maps and Thermal Boundary Conductance. *J. Phys. Chem. B* **2014**, *118*, 7818−7826.

(50) Xu, Y.; Leitner, D. M. Communication Maps of Vibrational Energy Transport in Photoactive Yellow Protein. *J. Phys. Chem. A* **2014**, *118*, 7280−7287.

(51) Agbo, J. K.; Gnanasekaran, R.; Leitner, D. M. Communication Maps: Exploring Energy Transport through Proteins and Water. *Isr. J. Chem.* **2014**, *54*, 1065−1073.

(52) Leitner, D. M. Frequency Resolved Communication Maps for Proteins and Other Nanoscale Materials. *J. Chem. Phys.* **2009**, *130*, 195101.

(53) Gnanasekaran, R.; Agbo, J. K.; Leitner, D. M. Communication Maps Computed for Homodimeric Hemoglobin: Computational Study of Water-Mediated Energy Transport in Proteins. *J. Chem. Phys.* **2011**, *135*, 065103.

(54) Gnanasekaran, R.; Xu, Y.; Leitner, D. M. Dynamics of Water Clusters Confined in Proteins: A Molecular Dynamics Simulation Study of Interfacial Waters in a Dimeric Hemoglobin. *J. Phys. Chem. B* **2010**, *114*, 16989−16996.

(55) Leitner, D. M. Water-Mediated Energy Dynamics in a Homodimeric Hemoglobin. *J. Phys. Chem. B* **2016**, *120*, 4019−4027.

(56) Boffi, A.; Chiancone, E. Evaluating Cooperativity in Dimeric Hemoglobins. *Methods Enzymol.* **2004**, *379*, 55−64.

(57) Royer, W. E.; Pardanani, A.; Gibson, Q. H.; Peterson, E. S.; Friedman, J. M. Ordered Water Molecules as Key Allosteric Mediators in a Cooperative Dimeric Hemoglobin. *Proc. Natl. Acad. Sci. U. S. A.* **1996**, *93*, 14526−14531.

(58) Kim, J. G.; Muniyappan, S.; Oang, K. Y.; Kim, T. W.; Yang, C.; Kim, K. H.; Kim, J.; Ihee, H. Cooperative Protein Structural Dynamics of Homodimeric Hemoglobin Linked to Water Cluster at Subunit Interface Revealed by Time-Resolved X-Ray Solution Scattering. *Struct. Dyn.* **2016**, *3*, 023610.

(59) Kim, K. H.; Muniyappan, S.; Oang, K. Y.; Kim, J. G.; Nozawa, S.; Sato, T.; Koshihara, S.; Henning, R.; Kosheleva, I.; Ki, H.; et al. Direct Observation of Cooperative Protein Structural Dynamics of Homodimeric Hemoglobin from 100 ps to 10 ms with Pump-Probe X-Ray Solution Scattering. *J. Am. Chem. Soc.* **2012**, *134*, 7001−7008.

(60) Laine, J. M.; Amat, M.; Morgan, B. R.; Royer, W. E.; Massi, F. Insight into the Allosteric Mechanism of Scapharca Dimeric Hemoglobin. *Biochemistry* **2014**, *53*, 7199−7210.

(61) Leitner, D. M.; Hyeon, C.; Reid, K. M. Water-Mediated Biomolecular Dynamics and Allostery. *J. Chem. Phys.* **2020**, *152*, 240901.

(62) Lee, Y.; Kim, S.; Choi, S.; Hyeon, C. Ultraslow Water-Mediated Transmembrane Interactions Regulate the Activation of A2a Adenosine Receptor. *Biophys. J.* **2016**, *111*, 1180−1191.

(63) Nguyen, P. H.; Park, S. M.; Stock, G. Nonequilibrium Molecular Dynamics Simulation of the Energy Transfer through a Peptide Helix. *J. Chem. Phys.* **2010**, *132*, 025102.

(64) Maier, J. A.; Martinez, C.; Kasavajhala, K.; Wickstrom, L.; Hauser, K. E.; Simmerling, C. Ff14sb: Improving the Accuracy of Protein Side Chain and Backbone Parameters from Ff99sb. *J. Chem. Theory Comput.* **2015**, *11*, 3696−3713.

(65) Case, D. A.; Betz, R. M.; Cerutti, D. S.; Cheatham, T. E.; Darden, T. A.; Duke, R. E.; Giese, T. J.; Gohlke, H.; Goetz, A. W.; Homeyer, N. et al. *Amber 2016*; University of California, San Francisco, 2016.

(66) Berendsen, H.; Postma, J.; vanGunsteren, W.; DiNola, A.; Haak, J. Molecular-Dynamics with Coupling to an External Bath. *J. Chem. Phys.* **1984**, *81*, 3684−90.

(67) Darden, T.; York, D.; Peterson, L. Particle Mesh Ewald: An N Log(N) Method for Ewald Sums in Large Systems. *J. Chem. Phys.* **1993**, *98*, 10089−10092.

(68) Nakayama, T.; Kousuke, Y.; Orbach, R. L. Dynamical Properties of Fractal Networks: Scaling, Numerical Simulations, and Physical Realizations. *Rev. Mod. Phys.* **1994**, *66*, 381−443.

(69) Alexander, S.; Orbach, R. Density of States of Fractals: 'Fractons'. *J. Phys., Lett.* **1982**, *43*, 625−631.

(70) Alexander, S.; Bernasconi, J.; Scheider, W. R.; Orbach, R. Excitation Dynamics in Random One-Dimensional Systems. *Rev. Mod. Phys.* **1981**, *53*, 175−198.

(71) Rammal, R.; Toulouse, G. Random Walks on Fractal Structures and Percolation Clusters. *J. Phys., Lett.* **1983**, *44*, 13−22.

(72) Yu, X.; Leitner, D. M. Anomalous Diffusion of Vibrational Energy in Proteins. *J. Chem. Phys.* **2003**, *119*, 12673−12679.

(73) Enright, M. B.; Yu, X.; Leitner, D. M. Hydration Dependence of the Mass Fractal Dimension and Anomalous Diffusion of Vibrational Energy in Proteins. *Phys. Rev. E* **2006**, *73*, 051905.

(74) Enright, M. B.; Leitner, D. M. Mass Fractal Dimension and the Compactness of Proteins. *Phys. Rev. E* **2005**, *71*, 011912.

(75) Tran, D. P.; Kitao, A. Kinetic Selection and Relaxation of the Intrinsically Disordered Region of a Protein Upon Binding. *J. Chem. Theory Comput.* **2020**, *16*, 2835−2845.

(76) Pandey, H. D.; Leitner, D. M. Small Saccharides as a Blanket around Proteins: A Computational Study. *J. Phys. Chem. B* **2018**, *122*, 7277−7285.

(77) Pandey, H. D.; Leitner, D. M. Influence of Thermalization on Thermal Conduction through Molecular Junctions: Computational Study of Peg Oligomers. *J. Chem. Phys.* **2017**, *147*, 084701.

(78) Pandey, H. D.; Leitner, D. M. Thermalization and Thermal Transport in Molecules. *J. Phys. Chem. Lett.* **2016**, *7*, 5062−5067.

(79) Leitner, D. M. Quantum Ergodicity and Energy Flow in Molecules. *Adv. Phys.* **2015**, *64*, 445−517.

(80) Gaskins, J. T.; Bulusu, A.; Giordano, A. J.; Duda, J. C.; Graham, S.; Hopkins, P. E. Thermal Conductance across Phosphonic Acid Molecules and Interfaces: Ballistic Versus Diffusive Vibrational Transport in Molecular Monolayers. *J. Phys. Chem. C* **2015**, *119*, 20931−20939.

(81) Majumdar, S.; Sierra-Suarez, J. A.; Schiffres, S. N.; Ong, W.-L.; Higgs, C. F.; McGaughey, A. J. H.; Malen, J. A. Vibrational Mismatch of Metal Leads Controls Thermal Conductance of Self-Assembled Monolayer Junctions. *Nano Lett.* **2015**, *15*, 2985−2991.

(82) Segal, D.; Agarwalla, B. K. Vibrational Heat Transport in Molecular Junctions. *Annu. Rev. Phys. Chem.* **2016**, *67*, 185−209.

(83) Stocker, K. M.; Neidhart, S. M.; Gezelter, J. D. Interfacial Thermal Conductance of Thiolate-Protected Gold Nanospheres. *J. Appl. Phys.* **2016**, *119*, 025106.

(84) Li, Q.; Strange, M.; Duchemin, I.; Donadio, D.; Solomon, G. C. A Strategy to Suppress Phonon Transport in Molecular Junctions Using Π-Stacked Systems. *J. Phys. Chem. C* **2017**, *121*, 7175−7182.

(85) Chen, R.; Sharony, I.; Nitzan, A. Local Atomic Heat Currents and Classical Interference in Single-Molecule Heat Conduction. *J. Phys. Chem. Lett.* **2020**, *11*, 4261−4268.

(86) Losego, M. D.; Grady, M. E.; Sottow, N. R.; Cahill, D. G.; Braun, P. V. Effects of Chemical Bonding on Heat Transport across Interfaces. *Nat. Mater.* **2012**, *11*, 502−506.